Check for updates

Geophysical Research Letters

RESEARCH LETTER
10.1029/2025GL119304

JWST Discovers the Vertical Structure of Uranus' Ionosphere

Paola I. Tiranti[1], H. Melin[1], L. Moore[2,3], E. M. Thomas[1], K. L. Knowles[1], T. S. Stallard[1], K. Roberts[2,3], and J. O'Donoghue[4]

[1]Northumbria University, School of Engineering, Physics and Mathematics, Newcastle, UK, [2]Boston University, Boston, MA, USA, [3]Center for Space Physics, Boston University, Boston, MA, USA, [4]Department of Meteorology, University of Reading, Reading, UK

Key Points:

- Vertical H_3^+ temperature, volumetric density and total emission profiles across all longitudes are measured at Uranus for the first time
- Temperatures peak between 3,000 and 4,000 km, showing limited temperature variability, and volumetric ion densities peak between 1,000 and 2,000 km
- A depletion in H_3^+ total emission and density is found along 190°–240°W, potentially indicative of magnetic field effects on the planet

Supporting Information:

Supporting Information may be found in the online version of this article.

Correspondence to:

P. I. Tiranti,
p.tiranti@northumbria.ac.uk

Citation:

Tiranti, P. I., Melin, H., Moore, L., Thomas, E. M., Knowles, K. L., Stallard, T. S., et al. (2026). JWST discovers the vertical structure of Uranus' ionosphere. *Geophysical Research Letters*, *53*, e2025GL119304. https://doi.org/10.1029/2025GL119304

Received 10 SEP 2025
Accepted 5 FEB 2026

© 2026. The Author(s).
This is an open access article under the terms of the Creative Commons Attribution License, which permits use, distribution and reproduction in any medium, provided the original work is properly cited.

Abstract On 19 January 2025, the James Webb Space Telescope (JWST) program #5073 observed Uranus for almost a full rotation with NIRSpec. We present the first ever vertical ionospheric profiles of H_3^+ temperature, volumetric density and total emission. Temperature profiles peak between 3,000–4,000 km at all longitudes. Densities peak near 1,000 km with values up to $(4.45 \pm 0.12) \times 10^8$ m^{-3}, lower than predicted by 1-D models. We identify two bright H_3^+ emission regions at 50°–110°W and 220°–290°W, near the auroral regions. A distinct emission and density depletion occurs between 190°–240°W, possibly reflecting magnetic topology influences, analogous to ionospheric dark regions at Jupiter. These results offer new insights into Uranus's upper atmosphere, confirm its long-term cooling trend (426 ± 2 K), and provide key constraints for ice giant ionospheric and magnetospheric modeling.

Plain Language Summary Uranus's upper atmosphere is one of the least understood in our Solar System, despite being critical for understanding how giant planets interact with their space environment. Using the James Webb Space Telescope, we observed Uranus for almost a full day and measured the vertical structure of its ionosphere - the charged layer of the atmosphere where aurorae form. Our results show that temperatures peak around 3,000–4,000 km above the planet, while ion densities peak near 1,000 km, and are significantly weaker than predicted by models. We also find two bright bands of auroral emission close to Uranus' magnetic poles, as well as a surprising region where both emission and density are depleted, likely linked to the unusual geometry of Uranus' tilted and offset magnetic field. These discoveries not only confirm that Uranus' upper atmosphere has been cooling for decades, but also reveal new structures shaped by its magnetic environment. Together, they provide critical benchmarks for future missions and improve our understanding of how giant planets (both in our Solar System and beyond) balance energy in their upper atmospheres.

1. Introduction

Uranus is a unique planet with a large axial tilt and an offset magnetic field (Ness et al., 1986). Given these characteristics and its ∼19 AU distance from the Sun, the resulting interaction between the space environment, magnetic field and atmosphere is complex and dynamic (Cao & Paty, 2017; Cowley, 2013). The upper atmosphere (defined above the homopause at ∼240–296 km, Moses et al. (2018); Joshi et al. (2026)) and auroral emissions have been observed in the ultraviolet (UV; Clarke et al., 1986; Herbert & Sandel, 1994; Herbert, 2009; Lamy et al., 2012, 2017, 2025), near-infrared (IR; e.g., Melin et al., 2019; Orton et al., 2014; Saunders et al., 2024; Thomas et al., 2023, 2025; Trafton et al., 1999; Trafton & Kaplan, 2025) and visible (Saunders et al., 2024).

IR observations often target H_3^+, a key molecular ion in giant planets ionospheres, including Uranus. As a quasi-thermalized ion, H_3^+ serves as a powerful remote diagnostic of upper atmospheric temperature and density structure (Miller et al., 2006, 2020). First detected at Uranus by Trafton et al. (1993), subsequent ground-based observations (Melin et al., 2019) have revealed long-term cooling of the upper atmosphere over three decades. However, these ground-based studies offer limited spatial resolution and sensitivity, preventing limb vertical profiles retrieval. Until now, no direct measurements of the vertical distribution of H_3^+ have been made at Uranus.

Vertical H_3^+ profiles reveal where energy is deposited, how it is redistributed, and how the upper atmosphere responds to drivers like solar radiation, particle precipitation, and magnetic field geometry. Vertical temperature gradients help constrain energy transport, while H_3^+ density peaks inform ion production and loss, key for both energy balance and long-term atmospheric escape. The first vertical profiles were retrieved at Jupiter's southern

19448007, 2026, 4, Downloaded from https://agupubs.onlinelibrary.wiley.com/doi/10.1029/2025GL119304 by Cochrane Russian Federation, Wiley Online Library on [19/02/2026]. See the Terms and Conditions (https://onlinelibrary.wiley.com/terms-and-conditions) on Wiley Online Library for rules of use; OA articles are governed by the applicable Creative Commons License

aurora using Keck (Lystrup et al., 2008), and later extended across latitudes and local times by ground-based and spacecraft observations (Dinelli et al., 2019; Kedziora-Chudczer et al., 2017; Migliorini et al., 2019, 2023; Stallard et al., 2015; Tiranti et al., 2025; Uno et al., 2014). At Saturn, only a single H_3^+ profile exists from Cassini (Stallard et al., 2012). Despite their limited number, these measurements have proven vital: as shown by a re-analysis of electron profiles from Pioneer 10/11, Voyager 1/2 and Galileo in Mendillo et al. (2022), vertical structure variations can explain ionospheric density asymmetries and constrain models of field aligned plasma transport (Agiwal et al., 2025; Moore et al., 2026).

Only two sets of vertical electron density profiles exist at Uranus, obtained by Voyager 2 (Lindal et al., 1987; Tyler et al., 1986). These profiles have similar shapes to those measured at Jupiter (Coffin et al., 2025; Mendillo et al., 2022), with distinct narrow layers and significant vertical variability with peak densities between 10^{10} and 10^{12} m^{-3} between 500 and 2,000 km altitude. At present, no vertical H_3^+ profiles have been measured at Uranus or Neptune, so models provide some preliminary expectations. Pre-Voyager modeling at Uranus predicted peak H_3^+ densities of $\sim 10^{10}$ m^{-3} at ~250 km altitude (McElroy, 1973). Chandler and Waite (1986) estimated an ionospheric peak at 1,200 km for H_3^+ of 1.5×10^9 m^{-3}. More recent efforts by Moore et al. (2019) modeled non-auroral regions, predicting H_3^+ to peak between 1,000 and 3,000 km ($\sim 10^9$ m^{-3}) which gradually decline toward higher altitudes. Their model adopted a Voyager 2-era temperature profile, relatively hot compared to present conditions, while long-term observations have shown a steady cooling over recent decades (Melin et al., 2011, 2013, 2019; Trafton & Kaplan, 2025). This decline in temperature reduces the H_2 scale height and could significantly reshape the ionospheric structure, as H_3^+ production depends on the ambient H_2 population.

Given the community's interest in a Uranus flagship mission (Simon et al., 2021), and the lack of observational constraints on the magnetospheric and ionospheric environments at the ice giants, we present the first H_3^+ vertical profiles as observed by the James Webb Space Telescope (JWST) at Uranus. The observations and the retrieval of vertical ionospheric profiles from the near-infrared spectra are detailed in Section 2, results are presented in Section 3 and discussed in Section 4. Finally, conclusions are given in Section 5.

2. Observations and Spectral Analysis

JWST General Observer program #5073 (PI H. Melin) observed Uranus for 15.4 hr (under a full rotation; 17.2 hr) on 2025-01-19 from 09:10 UT to 00:37 UT the following day. Using a 5-point cycling pattern to capture the limb, 20 observations were obtained. We use NIRSpec Integral Field Unit (IFU Jakobsen et al., 2022) with the F290LP/G395H filter/grating, covering the spectral regions between 2.87 and 5.14 μm capturing strong H_3^+ emission between 3.29 and 4.10 μm. The integration time per exposure was 6.1 min.

We define limb altitudes above the 1-bar pressure level according to the NASA Navigation and Ancillary Information Facility (NAIF; Acton, 1996). Limb latitudes and longitudes are defined as planetocentric latitudes and west longitudes, respectively, of the point on the limb closest to the pixel look vector. The observations covered all longitudes and latitudes available between 25°N and 25°S. We bin all spectra in 350 km altitude steps from 475 km to 5,025 km, computing the median per bin. Sub-pixel dithering and integration over many hours enable vertical resolution well below the nominal 1,400 km/spaxel. Here, due to Uranus' unusual geometry and coordinate conventions, we bin data by longitude rather than latitude. We adopt the Voyager-era Uranus Longitude System (Ness et al., 1986), which can be extended into the current era using Lamy et al. (2025), as per Melin et al. (2025).

To convert the observed line-of-sight (LOS) H_3^+ spectra to local volumetric spectra, which enables the retrieval of H_3^+ temperatures and volumetric densities, we apply a Tikhonov regularization technique (Tikhonov & Arsenin, 1977). This approach has been applied on a number of spacecraft data: Mars Express (Quémerais et al., 2006), MAVEN (Gröller et al., 2018) and Cassini (Koskinen et al., 2011), as well as on JWST/NIRSpec Fixed Slit (Denneulin et al., 2023) and IFU spectra (Tiranti et al., 2025). To control error growth and balance the signal-to-noise (S/N) ratio, we use a smoothing factor of $\lambda = 0.17$, chosen to provide minimal stabilization of the inversion while retaining an optimal vertical resolution. We quantify the uncertainty in the inversion and regularization process as specified in Supporting Information Text S1 and S2. Typical uncertainties remain under 10% up to 5,025 km, above which the profiles become unreliable.

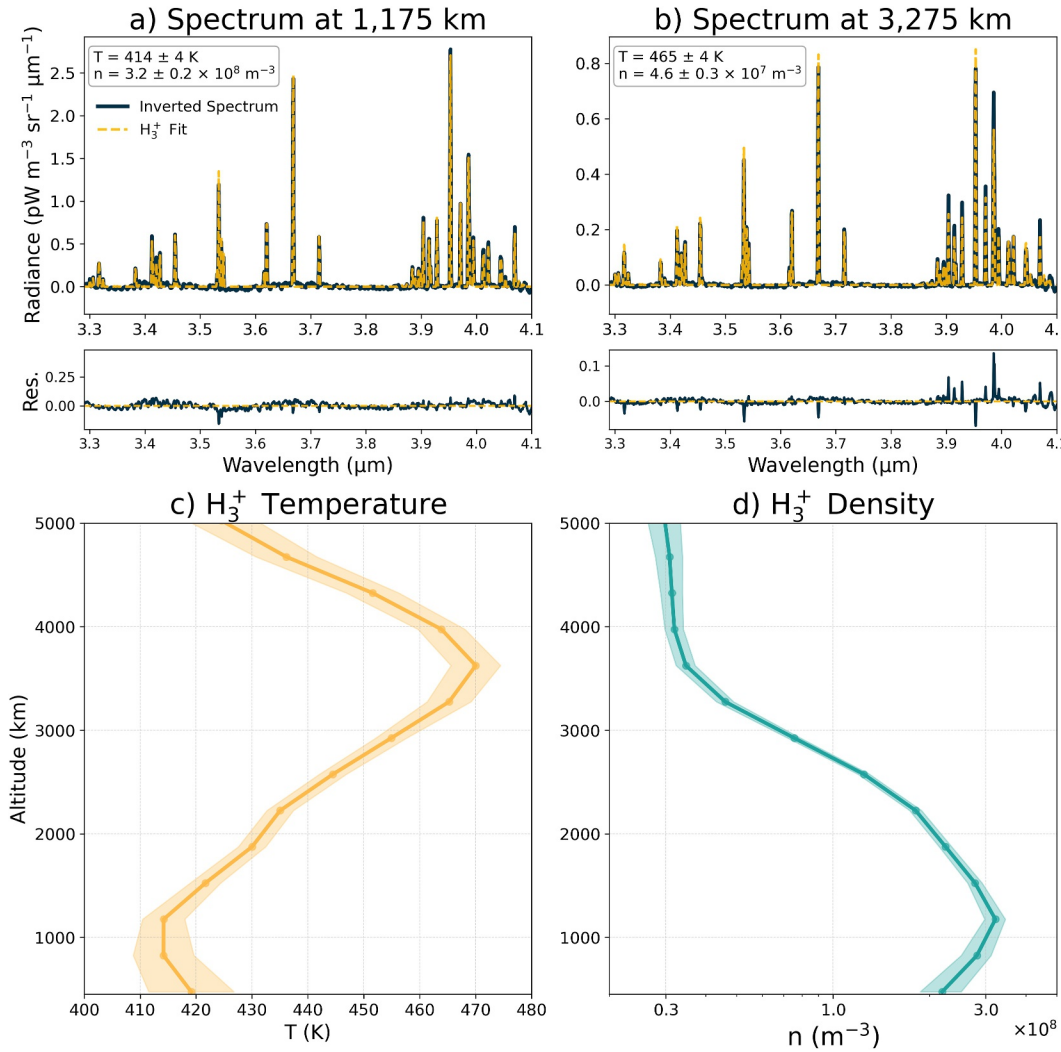

Figure 1. Examples of spectral fitting and vertical profiles. (a) Spectrum at 1,175 km, after LOS inversion (blue), as described in Section 2, and H_3^+ fit (yellow) from h3ppy fitting model (Melin, 2025). The residual is shown below (blue) against the 0-line (yellow). (b) Same as in panel (a) but at 3,275 km. (c) Global H_3^+ temperature profile derived by combining all latitudes and longitudes together. (d) Corresponding H_3^+ volumetric number density profile.

From the resulting inverted volumetric spectral profiles we fit the H_3^+ spectrum to obtain volumetric parameters at each altitude bin using the h3ppy fitting tool (Melin, 2025). From this procedure we obtain the local H_3^+ temperature and ion density, as well as the H_3^+ total emission (i.e., radiative loss). Examples of the spectral inversion and fitting at two different altitudes are shown in Figure 1a (1,175 km altitude) and Figure 1b (3,275 km altitude). We subsequently show the results from these fits as a function of altitude to produce global vertical profiles, as presented in Figures 1c and 1d.

3. Results

The globally averaged H_3^+ temperature profile in Figure 1c increases approximately linearly from 419 ± 7 K at 475 km to a peak of 470 ± 4 K at 3,625 km, and decreases steadily again toward higher altitudes. The overall vertical median temperature is 436 K (standard deviation, σ = 19 K, indicating variability). The global H_3^+ volumetric density profile (Figure 1d) peaks at 1,175 km at $(3.20 \pm 0.24) \times 10^8$ m^{-3}. Densities quickly decrease to a median of 3.20×10^7 m^{-3} above 3,500 km and median uncertainties of 0.20×10^7 m^{-3} at altitudes above this peak. By integrating these profiles, we retrieve a column integrated H_3^+ density of 6.6×10^{14} m^{-2} and temperature of 426 ± 2 K.

19448007, 2026, 4, Downloaded from https://agupubs.onlinelibrary.wiley.com/doi/10.1029/2025GL119304 by Cochrane Russian Federation, Wiley Online Library on [19/02/2026]. See the Terms and Conditions (https://onlinelibrary.wiley.com/terms-and-conditions) on Wiley Online Library for rules of use; OA articles are governed by the applicable Creative Commons License

19448007, 2026, 4, Downloaded from https://agupubs.onlinelibrary.wiley.com/doi/10.1029/2025GL119304 by Cochrane Russian Federation, Wiley Online Library on [19/02/2026]. See the Terms and Conditions (https://onlinelibrary.wiley.com/terms-and-conditions) on Wiley Online Library for rules of use; OA articles are governed by the applicable Creative Commons License

With full longitude coverage available, we extract vertical profiles every 10°W longitude across all available latitudes. Figures 2a, 2c and 2e show local H_3^+ temperatures, volumetric number densities and total emission, respectively, and Figures 2b, 2d and 2f show corresponding uncertainties. Temperature profiles in Figure 2a peak between 3,000–4,000 km up to 500 K, particularly across 0°–130°W. At lower altitudes, there is a slight temperature enhancement between 60°–100°W and between 230°–250°W, matching expected northern and southern auroral longitudes (Herbert, 2009). Median temperature uncertainties are 4 K, increasing with altitude, where the S/N is lower. Volumetric H_3^+ densities in Figure 2c peak between 1,000 km and 2,000 km across all longitudes, with a maximum of $(4.45 \pm 0.12) \times 10^8$ m^{-3} and $\sigma = 1.08 \times 10^8$ m^{-3}. Densities rapidly decrease above 2,500 km, reaching a minimum of $\sim 10^7$ m^{-3}. The median of the fitted density uncertainty is 3.90×10^6 m^{-3} (Figure 2d). H_3^+ total emission, in Figure 2e, peaks between 1,000 and 2,500 km, with two main bright regions between 50°–110°W and between 220°–290°W. Corresponding median of the fitted total emission uncertainty is 1.60×10^{-15} Wm^{-3} sr^{-1} (Figure 2f).

To investigate what primarily drives H_3^+ emissions at different altitudes across all longitudes, we calculate the Pearson correlation coefficients (p) between total emission and both temperature and density in Figure 2g. Below the H_3^+ density peak (~1,175 km), total emission correlates slightly more with temperature ($p = 0.5$) than with density ($p = 0.2$). However, above 1,000 km and below 3,000 km, emission correlates with density rather than temperature ($p = 0.6$ and $p = 0.2$, respectively). At mid-to-high altitudes (3,000–4,000 km), emission correlates with temperature ($p = 0.6$), showing little correlation with density ($p = 0.1$), suggesting that thermal processes dominate the emission at high altitudes (see Section 4).

In Figure 3, we explore more closely the physical parameters at low (blue; 475–1,175 km), mid (green; 1,525–2,225 km) and high (yellow; 3,275–3,975 km) altitudes as a function of longitude, to capture density and temperature peaks. At low altitudes, temperatures appear elevated at 60°–120°W and 230°–260°W (Figure 3a). Similar to Figure 2a, temperatures generally rise with increasing altitude, reaching their maximum of 490 ± 4 K at 115°W in the high altitudes. This altitude region also exhibits a temperature minimum (438 ± 3 K) between 200°–240°W. At a similar location (190°–240°W), a depletion in H_3^+ density is observed in the low and mid altitudes only (Figure 3b), where densities show a first extended enhancement of $\sim 3.50 \times 10^8$ m^{-3}. Densities then drop to a minimum of $\sim 2.00 \times 10^8$ m^{-3} at low altitudes and 1.56×10^8 m^{-3} at mid altitudes. A second density enhancement between 250°–290°W is observed after these minima, with the maximum density reaching 3.97×10^8 m^{-3} at low altitudes. H_3^+ total emission (Figure 3c) shows a coherent pattern across all three altitude bands. Emission peaks first between 50°–100°W, declines steadily to a minimum at 200°W and peaks again in a second emission enhancement between 240°–280°W.

We next investigate how H_3^+ parameters vary across different longitudinal regions, focusing on auroral and non-auroral sectors. Figures 4a and 4b show vertical H_3^+ temperature and density profiles, respectively, for five sectors defined by longitude: two profiles along longitudes where aurorae are expected (0°–112°W and 200°–251°W, defined as A1 and A2), two non-auroral profiles (113°–199°W and 252°–360°W, defined as NA1 and NA2) and a profile along the longitudes where we identified a decrease in emission and density in Figures 3b and 3c (190°–240°W, defined as Emission Dip: ED), as mapped in Figure 4c. Once again, as in Figure 2a, all five temperature profiles exhibit a clear peak between 3,000–4,000 km. The warmest region is A1, where the temperature reaches 475 ± 3 K at 3,625 km. In comparison, A2 peaks at 457 ± 2 K at 2,925 km, with a 18 K difference between the two auroral zones. The ED profile presents the coolest temperature peak, with a maximum of 456 ± 3 K at 3,275 km. Given the similar longitude sampling between the ED and A2 profiles, they appear quite similar. Despite this, the overall temperature profile morphology is consistent across all regions, with limited spatial variability. Similarly, density profiles (Figure 4b) show minimal differences too. H_3^+ density profiles peak just above 1,000 km with a mean of 3.18×10^8 m^{-3} ($\sigma = 2.54 \times 10^7$ m^{-3}), except for the ED profile that peaks at 825 km with a density of $(2.38 \pm 0.12) \times 10^8$ m^{-3}. A1 exhibits the highest median density at 1.30×10^8 m^{-3} (with a median uncertainty of 3.10×10^6 m^{-3}), while A2 presents a median density of 9.74×10^7 m^{-3} (median uncertainty is 2.93×10^6 m^{-3}), corresponding to 28.2% difference. The NA1 and NA2 profiles are almost identical in both temperature and density, indicating a largely uniform vertical structure outside the auroral regions.

To compare the vertical profiles derived here to those modeled by Moore et al. (2019), we extract a single non-auroral southern vertical profile by combining observations between 15°S and 25°S, across the longitude ranges 0°–30°W, 113°–199°W, and 252°–360°W, as mapped in Figure 4f. The temperature profile, shown in Figure 4d,

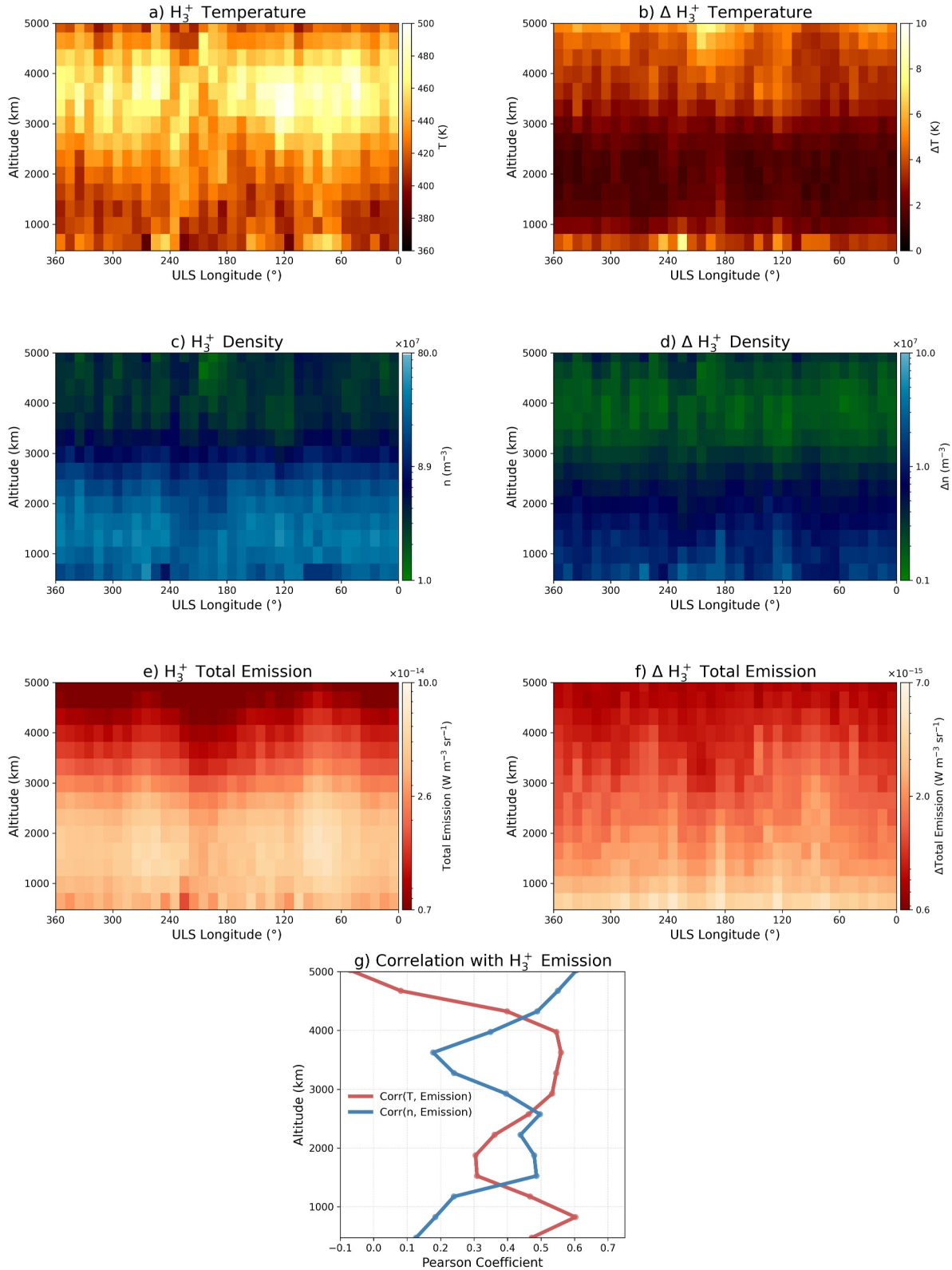

Figure 2. Maps of retrieved volumetric H_3^+ parameters binned every 10° longitudes and 350 km altitude. (a) H_3^+ measured temperatures with corresponding uncertainties in panel (b). (c) H_3^+ measured number densities with corresponding uncertainties in panel (d). (e) H_3^+ total emission with corresponding uncertainties in panel (f). (g) Pearson correlation of total H_3^+ emission with temperature (red) and density (blue), respectively, across all longitudes.

19448007, 2026, 4, Downloaded from https://agupubs.onlinelibrary.wiley.com/doi/10.1029/2025GL119304 by Cochrane Russian Federation, Wiley Online Library on [19/02/2026]. See the Terms and Conditions (https://onlinelibrary.wiley.com/terms-and-conditions) on Wiley Online Library for rules of use; OA articles are governed by the applicable Creative Commons License

10.1029/2025GL119304

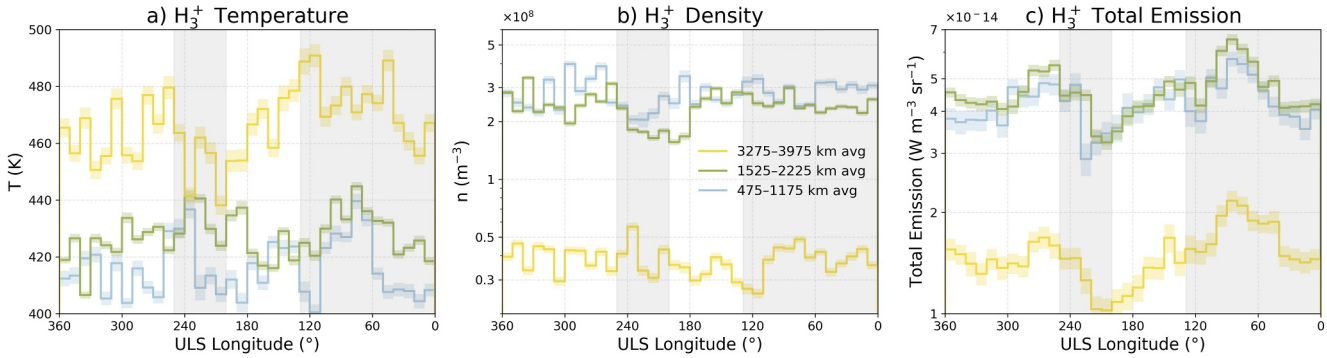

Figure 3. Morphology of H_3^+ parameters (a) temperature, (b) density, (c) total emission across longitudes for different altitude groups: low, 475–1,175 km (blue), mid, 1,525–2,225 km (green), and high 3,275–3,975 km (yellow). The shaded gray areas (0°–129° and 200°–250°W) indicate the longitudes where aurorae are expected (Herbert, 2009).

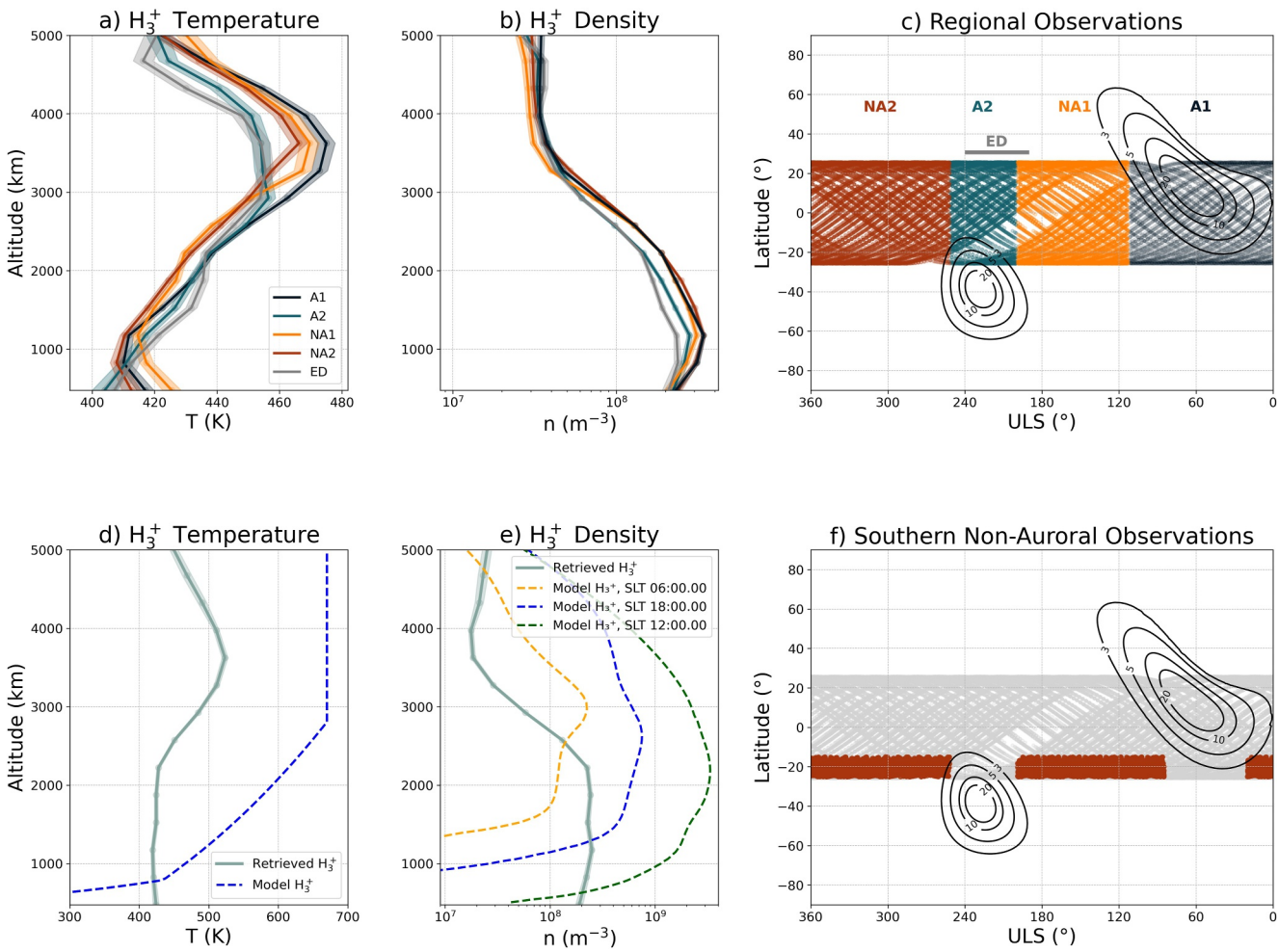

Figure 4. Vertical profiles in different regions. (a) and (b) H_3^+ temperature and number density, respectively, for auroral region 1 (A1, 0°–112°W, dark gray), auroral region 2 (A2, 200°–251°W, dark green), non auroral region 1 (NA1, 113°–199°W, orange), non auroral region 2 (NA2, 252°–360°W, brown), emission dip region (ED, 190°–240°W, light gray). (c) Limb data points projected on disk used for the different regional profiles, as described above, with L-shells contours from the Q3 model (Connerney et al., 1987). (d) H_3^+ temperature profile for all observations between 15°S–25°S across 0°–30°W, 113°–199°W, and 252°–360°W to focus on non-auroral data; and comparison with assumed model temperature (blue). (e) Corresponding number density profile (green) and modeled H_3^+ profile at solar local time (SLT) 06:00 (orange), 12:00 (green) and 18:00 (blue) adapted from Moore et al. (2019) at 20°S. (f) As panel (c) but for data points used to derive profiles in panel (d) and (e).

19448007, 2026, 4, Downloaded from https://agupubs.onlinelibrary.wiley.com/doi/10.1029/2025GL119304 by Cochrane Russian Federation, Wiley Online Library on [19/02/2026]. See the Terms and Conditions (https://onlinelibrary.wiley.com/terms-and-conditions) on Wiley Online Library for rules of use; OA articles are governed by the applicable Creative Commons License

peaks at 3,625 km with a maximum of 524 ± 4 K. The corresponding H_3^+ density profile is shown in Figure 4e, alongside model predictions for 06:00 (dawn), 12:00 (noon) and 18:00 (dusk) solar local time (SLT). These SLTs were selected since all our data come from above the limb, meaning the observations occur near the terminator, and to enable comparison with the predicted noon time maximum. To increase S/N and measurement accuracy, we combine all available southern non-auroral data. The retrieved H_3^+ density peaks at 1,175 km with a value of $(2.58 \pm 0.13) \times 10^8$ m^{-3}. In comparison, modeled densities peak at 2.24×10^8 m^{-3} at 2,970 km (dawn, broadly consistent with the retrieved value), 7.50×10^8 m^{-3} at 2,624 km (dusk, roughly three times higher), and 3.35×10^9 m^{-3} at 2,197 km (noon, more than an order of magnitude higher).

4. Discussion

Here, we present the first vertical volumetric H_3^+ ion temperature and density profiles at Uranus. The vertical and longitudinal temperature profiles reinforce and extend the long-term cooling trend of Uranus' upper atmosphere observed since 1992. The column-weighted temperature is 426 ± 2 K (Figure 1c), cooler than any values reported in Melin et al. (2019), though slightly higher than JWST disk-averaged observations (415 K, Melin et al. (2025)), likely due to our data set focusing on the dynamic terminator regions, that may produce slightly higher temperatures than the average across the full sunlit disk. The cooling trend has been attributed to reduced solar wind power (Masters et al., 2024), although this remains debated (Jasinski et al., 2025). Our observed profiles show a modest temperature enhancement between 3,000–4,000 km, followed by a reduced cooling rate at higher altitudes, which is consistent with heating occurring below or near the exobase (likely around ∼4,000 km in the present epoch, compared to ∼6,500 km during the Voyager-cera; Joshi et al., 2025) (discussed below). The observed temperatures suggest that Uranus' thermospheric energy balance cannot be explained by collisional heat transfer alone. In a purely collisional regime strong spatial gradients and cooling with altitude would be expected, as energy is deposited locally and transferred efficiently to neutrals. The weak longitudinal gradients and elevated temperatures at high altitude imply additional heating or redistribution processes such as gravity wave dissipation or thermal conduction. Temperatures remain confined to 380–480 K across all longitudes (Figure 2a), consistent with JWST and ground-based observations (Melin et al., 2025; Thomas et al., 2023), which observed limited variability across the disk. Auroral heating at Uranus may be less pronounced than the several-hundred-Kelvin enhancements observed in the polar regions of Jupiter and Saturn (Brown et al., 2020; O'Donoghue et al., 2021; Roberts et al., 2025) or, alternatively, transport may be more efficient. A latitudinal temperature gradient was noted by Melin et al. (2025), which may explain the higher peak temperature seen in Figure 4d compared to those in Figure 4a.

The auroral enhancements in total H_3^+ emission (Figure 3c) extend over significant longitudes ranges (∼50°), while both JWST and HST commonly show compact, spot-like brightenings (e.g., Lamy et al., 2025; Melin et al., 2025). The mean A1 density (Figure 4b) is only ∼0.4% higher than the mean of NA1 and NA2. A small density contrast does not imply weak particle precipitation: enhanced ionization can increase recombination with electrons, limiting H_3^+ densities, consistent with preferential energetic proton precipitation at Uranus' north magnetic pole (Acevski & Masters, 2024). Figure 4c includes only a very small portion of the southern auroral region, while covering the northern sector more completely, further reducing apparent contrasts. Future modeling work should include Pedersen conductivity (to localize Joule heating) and co-located electron density constraints; we flag conductivity estimates from our retrieved profiles as a priority for future model-data work.

At all longitudes, the vertical H_3^+ temperature profiles show a distinct peak between 3,000–4,000 km (Figures 2a and 4d), but they only vary by about ∼100 K in altitude. The temperature profiles derived from the Voyager 2 UV occultations (Herbert et al., 1987) vary ∼600 K over similar altitudes, but do display an almost linear increase toward a maximum at around ∼5,000 km. Recent reanalyzes of ground-based stellar occultations suggest that the lower thermosphere is cooler than the Voyager 2 retrievals and that the stratosphere–thermosphere boundary could lie higher in altitude than previously believed (Saunders et al., 2024). Generally, the exospheric temperature profile is expected to be constant with altitude (isothermal), which is not seen here. This may be due to non-Local Thermodynamic Equilibrium (LTE) effects in the H_3^+ emission that become particularly important when the H_2 density is low (i.e., at high altitude; Melin et al., 2005). The model by Moore et al. (2019) has an H_2 density of ∼10^{15} m^{-3} at 3,000 km, which gives a non-LTE population ratio (the fraction of H_3^+ ν_2 levels depopulated relative to LTE) of ∼0.6 (Miller et al., 2013, Table 6), which reduces to ∼0.1 at 4,000 km where the H_2 density is ∼10^{14} m^{-3}.

19448007, 2026, 4, Downloaded from https://agupubs.onlinelibrary.wiley.com/doi/10.1029/2025GL119304 by Cochrane Russian Federation, Wiley Online Library on [19/02/2026]. See the Terms and Conditions (https://onlinelibrary.wiley.com/terms-and-conditions) on Wiley Online Library for rules of use; OA articles are governed by the applicable Creative Commons License

19448007, 2026, 4, Downloaded from https://agupubs.onlinelibrary.wiley.com/doi/10.1029/2025GL119304 by Cochrane Russian Federation, Wiley Online Library on [19/02/2026]. See the Terms and Conditions (https://onlinelibrary.wiley.com/terms-and-conditions) on Wiley Online Library for rules of use; OA articles are governed by the applicable Creative Commons License

This likely indicates that non-LTE effects are important at high altitudes at Uranus, and shapes the high altitude profiles (>3,000 km) derived here.

Recent HST Ly-α observations (Joshi et al., 2025) reveal a potential gravitationally bound hot hydrogen population in Uranus' extended exosphere, suggesting additional energy sources beyond solar EUV. Within our altitude range, we recover distinct vertical temperature structure: at low/mid altitudes, temperatures vary by ∼40 K with longitude; at high altitudes the range is ∼60 K (Figure 3a). Given the dawn/dusk bias in our limb observations, photoionization and hence photoelectron production peak at significantly higher altitudes than at noon; model calculations for JWST-era geometry place the primary photoelectron heating near ∼4,000 km (Moore et al., 2019). This naturally produces a modest temperature bump at this altitude, which decreases before rising at higher altitudes as plasma decouples from neutrals. The low variability (∼50 K), suggests limited auroral Joule heating or efficient global energy redistribution over short timescales. However, Uranus remains part of the broader "giant planet energy crisis," where the upper atmosphere is observed to be much hotter than expected based on solar input. Modeling at Jupiter have suggested that the offset magnetic field can provide significant ion drag that enables equator-ward transport of auroral energy (Müller-Wodarg et al., 2025). Whilst similar modeling is required at Uranus, such transport could also be important here.

The vertical distribution of H_3^+ number density reported in Figures 2c and 3b appears largely uniform across longitudes, except for a localized decrease in density around 190°–240°W just above the H_3^+ peak, matching a depletion in H_3^+ emission at similar longitudes (Figure 3c). The lower densities in the ED region may be similar to the reduced H_3^+ intensities observed at equatorial latitudes at Jupiter, linked to variations in magnetic field topology (Knowles et al., 2025; Stallard et al., 2018). More recently, a comparable feature—described as a polar chevron—has been identified and associated with a depletion in H_3^+ column density near the magnetic dip equator (Melin et al., 2025). This structure has been observed mainly in the geometric southern pole, outside the latitudes covered here. From the Pearson coefficients (Figure 2g), we infer that the dominant driver of H_3^+ total emission variability depends on altitude, reflecting thermal excitation versus ion production dominance at different altitudes. Indeed, temperature drives variations in the emissions at high altitudes, while number density is more important around the peak density region and affects total H_3^+ emissions at low altitudes. For the ED profile in particular (Figure 4b) the density peak is ∼25% lower than the mean between all the other regions' peaks, with $\sigma = 2.54 \times 10^7$ m^{-3}.

The H_3^+ number density profile in Figure 1d peaks at 1,175 km with a value of $(3.20 \pm 0.24) \times 10^8$ m^{-3}, within the altitude range predicted by Chandler and Waite (1986) (∼1,200 km). However, our measured densities are approximately one order of magnitude lower than their peak values (1.5×10^9 m^{-3}) and below values from the Moore et al. (2019) 1-D calculations. Several factors plausibly contribute:

- Our profiles are extracted primarily near the terminator (20°S, sub-solar latitude ∼67.7°N), whereas the Moore et al. (2019) noon time examples used different sub-solar latitude (e.g., 39°S) and latitudes. Updated runs for JWST-era geometry show lower dawn/dusk densities and peak altitudes shifted upward, moving the models closer to our densities, although with morphological differences.
- A major source of uncertainty lies in the conversion rate from H^+ to H_3^+ via vibrationally excited H_2, which regulates recombination efficiency and hence H_3^+ densities, for which no observational constraints exist at Uranus. Moore et al. (2019) estimate this by scaling Jupiter's H_2 ($v \geq 4$) distribution, this may overestimate vibrational populations in Uranus's cooler thermosphere.
- Moore et al. (2019) adopted near-vertical field lines to justify vertical transport. At Uranus's highly tilted field, reduced vertical transport will alter the balance between electron and ion populations, leading to relatively lower H_3^+ densities than the model case, with a cooler thermosphere further reducing the scale height and shifting H_3^+ peaks to lower altitudes.
- Longitudinal/SLT averaging likely explain why the column-integrated densities (6.6×10^{14} m^{-2}) are approximately three times smaller than what is typically derived from disk-averaged observations (e.g., Melin et al., 2011).

The vertical H_3^+ temperature and density profiles derived here offer a new view of Uranus' ionosphere and highlight key constraints for future ionospheric models. Future in-situ measurements from an orbiter or atmospheric probe will be essential to fully characterize Uranus' complex upper atmosphere and resolve the outstanding questions raised by remote observations.

5. Conclusions

We have reported the first observations of H_3^+ vertical profiles up to 5,000 km captured by JWST/NIRSpec on 2025-01-19 between 25°N and 25°S across all longitudes. We measure a H_3^+ temperature peak at 3,625 km of 470 ± 4 K. Our derived temperatures broadly match recent ground-based and JWST observations, establishing that the long-term cooling of Uranus' upper atmosphere has continued.

Across all observations every 10° longitudes, we observe persistent temperature peaks between 3,000 and 4,000 km. Whilst the spatial coverage of the southern aurora is limited, we observe an enhancement in both H_3^+ temperature (tens of K) and density at the northern aurora (0°–120°W), indicating both auroral heating and particle impact ionization. H_3^+ number densities peak just above 1,000 km reaching a maximum of 4.45×10^8 m^{-3} and fall to $\sim 10^7$ m^{-3} above 2,000 km. These values are lower in both density and altitude than predicted by 1-D models. This could be due to a number of factors such as assumed model temperature and consequent over-estimation of H_2 vibrational population, and magnetic field geometry.

The vertical H_3^+ profiles derived here offer a new view of Uranus' ionosphere and provide critical benchmarks for future ionospheric and magnetospheric models. These measurements represent the most detailed characterization of Uranus' infrared vertical upper atmosphere to date. Future in-situ measurements from an orbiter or atmospheric probe will be essential to fully characterize Uranus' complex upper atmosphere and deepen our understanding of ice giant atmospheres relative to Jupiter, Saturn, and the growing exoplanets' population.

Conflict of Interest

The authors declare no conflicts of interest relevant to this study.

Data Availability Statement

The h3ppy fitting tool is an open-source fitting procedure (Melin, 2025) producing H_3^+ temperatures, densities and radiances, available in the Python programming language at https://pypi.org/project/h3ppy/. Results are stored in .fits files with all fitted values as function of longitude, local-time, latitude and altitude, along with corresponding uncertainties, all available on Zenodo via Tiranti (2025).

Acknowledgments
P.I.T. was funded by UK Science and Technology Facilities Council (STFC) Studentship ST/X508548/2. H.M. was supported by the STFC James Webb Fellowship (ST/W001527/2) at Northumbria University, UK. L.M. was supported Program number JWST-GO-05073.002-A via STScI/NASA contract NAS5- 03127. E.M.T. and T.S.S. were supported by an STFC Consolidated Grant (ST/W00089X/1) at Northumbria University, UK. K.L.K. was supported by a Northumbria University Research Studentship. K.R was supported by NASA FINESST Grant 80NSSC23K1637. J.O.D. was supported by the STFC Ernest Rutherford Fellowship (ST/X003426/1) at the University of Reading, UK.

References

Acevski, M., & Masters, A. (2024). Enhanced precipitation of energetic protons due to Uranus' asymmetric magnetic field. *Geophysical Research Letters*, *51*(24), e2024GL112281. https://doi.org/10.1029/2024GL112281

Acton, C. H. (1996). Ancillary data services of NASA's Navigation and ancillary Information Facility. *Planetary and Space Science*, *44*(1), 65–70. https://doi.org/10.1016/0032-0633(95)00107-7

Agiwal, O., Moore, L., Bloch, T., Coffin, D., Felici, M., Knowles, K. L., et al. (2025). Unraveling Jupiter's enigmatic ionosphere: Evidence of magnetically-controlled wind-driven dynamics. *Geophysical Research Letters*, *52*(24), e2025GL119171. https://doi.org/10.1029/2025GL119171

Brown, Z., Koskinen, T., Müller-Wodarg, I., West, R., Jouchoux, A., & Esposito, L. (2020). A pole-to-pole pressure–temperature map of Saturn's thermosphere from Cassini Grand Finale data. *Nature Astronomy*, *4*(9), 872–879. https://doi.org/10.1038/s41550-020-1060-0

Cao, X., & Paty, C. (2017). Diurnal and seasonal variability of Uranus's magnetosphere. *Journal of Geophysical Research: Space Physics*, *122*(6), 6318–6331. https://doi.org/10.1002/2017JA024063

Chandler, M., & Waite, J. (1986). The ionosphere of Uranus: A myriad of possibilities. *Geophysical Research Letters*, *13*(1), 6–9. https://doi.org/10.1029/GL013i001p00006

Clarke, J., Durrance, S., Atreya, S., Barnes, A., Belcher, J., Festou, M., et al. (1986). Continued observations of the H Ly α emission from Uranus. *Journal of Geophysical Research*, *91*(A8), 8771–8781. https://doi.org/10.1029/JA091iA08p08771

Coffin, D. A., Withers, P., Agiwal, O., Buccino, D., Parisi, M., Park, R. S., et al. (2025). Juno-Derived electron density profiles of the high-latitude jovian ionosphere. *Journal of Geophysical Research: Space Physics*, *130*(6), e2025JA033754. https://doi.org/10.1029/2025JA033754

Connerney, J., Acuña, M. H., & Ness, N. F. (1987). The magnetic field of Uranus. *Journal of Geophysical Research*, *92*(A13), 15329–15336. https://doi.org/10.1029/JA092iA13p15329

Cowley, S. (2013). Response of Uranus' auroras to solar wind compressions at equinox. *Journal of Geophysical Research: Space Physics*, *118*(6), 2897–2902. https://doi.org/10.1002/jgra.50323

Denneulin, L., Guilbert-Lepoutre, A., Langlois, M., Thiébaut, E., Holler, B., Ferruit, P., et al. (2023). An improved spectral extraction method for JWST/NIRSpec fixed slit observations. *Astronomy and Astrophysics*, *679*, A63. https://doi.org/10.1051/0004-6361/202346998

Dinelli, B., Adriani, A., Mura, A., Altieri, F., Migliorini, A., & Moriconi, M. (2019). JUNO/JIRAM's view of Jupiter's H3+ emissions. *Philosophical transactions of the Royal Society A*, *377*(2154), 20180406. https://doi.org/10.1098/rsta.2018.0406

Gröller, H., Montmessin, F., Yelle, R., Lefèvre, F., Forget, F., Schneider, N., & Jain, S. (2018). MAVEN/IUVS stellar occultation measurements of Mars atmospheric structure and composition. *Journal of Geophysical Research: Planets*, *123*(6), 1449–1483. https://doi.org/10.1029/2017JE005466

Herbert, F. (2009). Aurora and magnetic field of Uranus. *Journal of Geophysical Research*, *114*(A11). https://doi.org/10.1029/2009JA014394

19448007, 2026, 4, Downloaded from https://agupubs.onlinelibrary.wiley.com/doi/10.1029/2025GL119304 by Cochrane Russian Federation, Wiley Online Library on [19/02/2026]. See the Terms and Conditions (https://onlinelibrary.wiley.com/terms-and-conditions) on Wiley Online Library for rules of use; OA articles are governed by the applicable Creative Commons License

Herbert, F., & Sandel, B. (1994). The Uranian aurora and its relationship to the magnetosphere. *Journal of Geophysical Research*, *99*(A3), 4143–4160. https://doi.org/10.1029/93JA02673

Herbert, F., Sandel, B., Yelle, R., Holberg, J., Broadfoot, A., Shemansky, D., et al. (1987). The upper atmosphere of Uranus: EUV occultations observed by Voyager 2. *Journal of Geophysical Research*, *92*(A13), 15093–15109. https://doi.org/10.1029/JA092iA13p15093

Jakobsen, P., Ferruit, P., de Oliveira, C. A., Arribas, S., Bagnasco, G., Barho, R., et al. (2022). The Near-Infrared Spectrograph (NIRSpec) on the James webb space Telescope- I. Overview of the instrument and its capabilities. *Astronomy and Astrophysics*, *661*, A80. https://doi.org/10.1051/0004-6361/202142663

Jasinski, J. M., Melin, H., Sinclair, J. A., Zomerdijk-Russell, S., Achilleos, N., & Paty, C. (2025). Uranus' long-term thermospheric cooling is unlikely to be primarily driven by the solar wind. *Geophysical Research Letters*, *52*(24), e2025GL119362. https://doi.org/10.1029/2025GL119362

Joshi, S., Roth, L., Chaufray, J.-Y., Gladstone, R., Ivchenko, N., Strobel, D., & Lamy, L. (2026). Probing methane in Uranus' upper stratosphere using HST observations of the 1280 Å Raman feature. *Astronomy and Astrophysics*, *705*, A109. https://doi.org/10.1051/0004-6361/202556779

Joshi, S., Roth, L., Gladstone, R., Ivchenko, N., Pryor, W., & Lamy, L. (2025). Uranus' hydrogen upper atmosphere: Insights from pre-and post-equinox HST Lyman-α images. *Astronomy and Astrophysics*, *693*, A231. https://doi.org/10.1051/0004-6361/202450719

Kedziora-Chudczer, L., Cotton, D., Kedziora, D., & Bailey, J. (2017). The 2 μm spectrum of the auroral emission in the polar regions of Jupiter. *Icarus*, *294*, 156–171. https://doi.org/10.1002/2015JA021097

Knowles, K., Stallard, T., O'Donoghue, J., Moore, L., Agiwal, O., Melin, H., et al. (2025). Magnetic silhouettes in Jupiter's non-auroral ionosphere. *Journal of Geophysical Research: Space Physics*, *130*(5), e2025JA033868. https://doi.org/10.1029/2025JA033868

Koskinen, T., Yelle, R., Snowden, D., Lavvas, P., Sandel, B., Capalbo, F., et al. (2011). The mesosphere and lower thermosphere of Titan revealed by Cassini/UVIS stellar occultations. *Icarus*, *216*(2), 507–534. https://doi.org/10.1016/j.icarus.2011.09.022

Lamy, L., Prange, R., Berthier, J., Tao, C., Kim, T., Roth, L., et al. (2025). A new rotation period and longitude system for Uranus. *Nature Astronomy*, *9*(5), 1–8. https://doi.org/10.1038/s41550-025-02492-z

Lamy, L., Prangé, R., Hansen, K., Clarke, J., Zarka, P., Cecconi, B., & others (2012). Earth-based detection of Uranus' aurorae. *Geophysical Research Letters*, *39*(7). https://doi.org/10.1029/2012GL051312

Lamy, L., Prangé, R., Hansen, K., Tao, C., Cowley, S. W. H., Stallard, T., et al. (2017). The aurorae of Uranus past equinox. *Journal of Geophysical Research: Space Physics*, *122*(4), 3997–4008. https://doi.org/10.1002/2017JA023918

Lindal, G. F., Lyons, J., Sweetnam, D., Eshleman, V., Hinson, D. P., & Tyler, G. L. (1987). The atmosphere of Uranus: Results of radio occultation measurements with Voyager 2. *Journal of Geophysical Research*, *92*(A13), 14987–15001. https://doi.org/10.1029/JA092iA13p14987

Lystrup, M., Miller, S., Russo, N. D., Vervack, R., & Stallard, T. (2008). First vertical ion density profile in Jupiter's auroral atmosphere: Direct observations using the Keck II telescope. *The Astrophysical Journal*, *677*(1), 790–797. https://doi.org/10.1086/529509

Masters, A., Szalay, J., Zomerdijk-Russell, S., & Kao, M. (2024). Solar wind power likely governs Uranus' thermosphere temperature. *Geophysical Research Letters*, *51*(22), e2024GL111623. https://doi.org/10.1029/2024GL111623

McElroy, M. B. (1973). The ionospheres of the major planets. *Space Science Reviews*, *14*(3), 460–473. https://doi.org/10.1007/BF00214756

Melin, H. (2025). h3ppy: An open-source Python package for modelling and fitting spectra. *Journal of Open Source Software*, *10*(107), 7536. https://doi.org/10.21105/joss.07536

Melin, H., Fletcher, L., Stallard, T., Miller, S., Trafton, L., Moore, L., et al. (2019). The H3+ ionosphere of Uranus: Decades-long cooling and local-time morphology. *Philosophical transactions of the Royal Society A*, *377*(2154), 20180408. https://doi.org/10.1098/rsta.2018.0408

Melin, H., Fletcher, L. N., Hammel, H. B., Milam, S. N., Moore, L., Stallard, T. S., et al. (2025). The ionosphere of Uranus as revealed by JWST. *Geophysical Research Letters*, *52*(22), e2025GL118301. https://doi.org/10.1029/2025GL118301

Melin, H., Miller, S., Stallard, T., & Grodent, D. (2005). Non-LTE effects on emission in the Jovian upper atmosphere. *Icarus*, *178*(1), 97–103. https://doi.org/10.1016/j.icarus.2005.04.016

Melin, H., Stallard, T., Miller, S., Trafton, L., Encrenaz, T., & Geballe, T. R. (2011). Seasonal variability in the ionosphere of Uranus. *The Astrophysical Journal*, *729*(2), 134. https://doi.org/10.1088/0004-637X/729/2/134

Melin, H., Stallard, T. S., Miller, S., Geballe, T. R., Trafton, L. M., & O'Donoghue, J. (2013). Post-equinoctial observations of the ionosphere of Uranus. *Icarus*, *223*(2), 741–748. https://doi.org/10.1016/j.icarus.2013.01.012

Mendillo, M., Narvaez, C., Moore, L., & Withers, P. (2022). Jupiter's enigmatic ionosphere: Electron density profiles from the Pioneer, Voyager, and Galileo radio occultation experiments. *Journal of Geophysical Research: Planets*, *127*(3), e2021JE007169. https://doi.org/10.1029/2021JE007169

Migliorini, A., Dinelli, B., Castagnoli, C., Moriconi, M., Altieri, F., Atreya, S., et al. (2023). First observations of CH4 and Spatially resolved emission layers at Jupiter equator, as seen by JIRAM/Juno. *Journal of Geophysical Research: Planets*, *128*(3), e2022JE007509. https://doi.org/10.1029/2022JE007509

Migliorini, A., Dinelli, B., Moriconi, M., Altieri, F., Adriani, A., Mura, A., et al. (2019). H3+ characteristics in the Jupiter atmosphere as observed at limb with Juno/JIRAM. *Icarus*, *329*, 132–139. https://doi.org/10.1016/j.icarus.2019.04.003

Miller, S., Stallard, T., Smith, C., Millward, G., Melin, H., Lystrup, M., & Aylward, A. (2006). H3+: The driver of giant planet atmospheres. *Philosophical Transactions of the Royal Society A: Mathematical, Physical and Engineering Sciences*, *364*(1848), 3121–3137. https://doi.org/10.1098/rsta.2006.1877

Miller, S., Stallard, T., Tennyson, J., & Melin, H. (2013). Cooling by H3+ emission. *Journal of Physical Chemistry A*, *117*(39), 9770–9777. https://doi.org/10.1021/jp312468b

Miller, S., Tennyson, J., Geballe, T. R., & Stallard, T. (2020). Thirty years of H3+ astronomy. *Reviews of Modern Physics*, *92*(3), 035003. https://doi.org/10.1103/RevModPhys.92.035003

Moore, L., Melin, H., O'Donoghue, J., Stallard, T., Moses, J., Galand, M., et al. (2019). Modelling H3+ in planetary atmospheres: Effects of vertical gradients on observed quantities. *Philosophical Transactions of the Royal Society A*, *377*(2154), 20190067. https://doi.org/10.1098/rsta.2019.0067

Moore, L., Melin, H., Stallard, T., O'Donoghue, J., Roberts, K., Tiranti, P. I., et al. (2026). Photochemistry in Jupiter's ionosphere: Insights from simultaneous H 3+ and electron density observations during Juno Perijove 54. *The Planetary Science Journal*, *7*(1), 25. https://doi.org/10.3847/PSJ/ae2f49

Moses, J. I., Fletcher, L. N., Greathouse, T. K., Orton, G. S., & Hue, V. (2018). Seasonal stratospheric photochemistry on Uranus and Neptune. *Icarus*, *307*, 124–145. https://doi.org/10.1016/j.icarus.2018.02.004

Müller-Wodarg, I. C. F., Iñurrigarro, P., Moore, L., Koskinen, T. T., & Medvedev, A. S. (2025). Temperatures of Jupiter's upper atmosphere: The role of the planetary magnetic field. *The Astrophysical Journal Letters*, *990*(1), L22. https://doi.org/10.3847/2041-8213/adfa21

Ness, N. F., Acuña, M. H., Behannon, K. W., Burlaga, L. F., Connerney, J. E., Lepping, R. P., & Neubauer, F. M. (1986). Magnetic fields at Uranus. *Science*, *233*(4759), 85–89. https://doi.org/10.1126/science.233.4759.85

19448007, 2026, 4, Downloaded from https://agupubs.onlinelibrary.wiley.com/doi/10.1029/2025GL119304 by Cochrane Russian Federation, Wiley Online Library on [19/02/2026]. See the Terms and Conditions (https://onlinelibrary.wiley.com/terms-and-conditions) on Wiley Online Library for rules of use; OA articles are governed by the applicable Creative Commons License

O'Donoghue, J., Moore, L., Bhakyapaibul, T., Melin, H., Stallard, T., Connerney, J., & Tao, C. (2021). Global upper-atmospheric heating on Jupiter by the polar aurorae. *Nature*, *596*(7870), 54–57. https://doi.org/10.1038/s41586-021-03706-w

Orton, G. S., Fletcher, L. N., Moses, J. I., Mainzer, A. K., Hines, D., Hammel, H. B., et al. (2014). Mid-infrared spectroscopy of Uranus from the Spitzer infrared spectrometer: 1. Determination of the mean temperature structure of the upper troposphere and stratosphere. *Icarus*, *243*, 494–513. https://doi.org/10.1016/j.icarus.2014.07.010

Quémerais, E., Bertaux, J.-L., Korablev, O., Dimarellis, E., Cot, C., Sandel, B. R., & Fussen, D. (2006). Stellar occultations observed by SPICAM on Mars express. *Journal of Geophysical Research*, *111*(E9). https://doi.org/10.1029/2005JE002604

Roberts, K., Moore, L., O'Donoghue, J., Melin, H., Stallard, T., Knowles, K. L., et al. (2025). Spatiotemporal variations of temperature in Jupiter's upper atmosphere. *The Planetary Science Journal*, *6*(4), 92. https://doi.org/10.3847/PSJ/adc09b

Saunders, W. R., Person, M. J., Withers, P., French, R. G., & Tubthong, C. (2024). The upper atmosphere of Uranus from stellar occultations. II. Revised temperatures in the upper stratosphere and lower thermosphere. *The Planetary Science Journal*, *5*(11), 247. https://doi.org/10.3847/PSJ/ad7c4d

Simon, A., Nimmo, F., & Anderson, R. (2021). *Uranus orbiter and probe: Journey to an ice giants system*. National Aeronautics and Space Administration.

Stallard, T. S., Burrell, A. G., Melin, H., Fletcher, L. N., Miller, S., Moore, L., et al. (2018). Identification of Jupiter's magnetic equator through H3+ ionospheric emission. *Nature Astronomy*, *2*(10), 773–777. https://doi.org/10.1038/s41550-018-0523-z

Stallard, T. S., Melin, H., Miller, S., Badman, S. V., Baines, K. H., Brown, R. H., et al. (2015). Cassini VIMS observations of H3+ emission on the nightside of Jupiter. *Journal of Geophysical Research: Space Physics*, *120*(8), 6948–6973. https://doi.org/10.1002/2015ja021097

Stallard, T. S., Melin, H., Miller, S., Badman, S. V., Brown, R. H., & Baines, K. H. (2012). Peak emission altitude of Saturn's H3+ aurora. *Geophysical Research Letters*, *39*(15). https://doi.org/10.1029/2012GL052806

Thomas, E. M., Melin, H., Stallard, T. S., Chowdhury, M. N., Wang, R., Knowles, K., & Miller, S. (2023). Detection of the infrared aurora at Uranus with Keck-NIRSPEC. *Nature Astronomy*, *7*(12), 1473–1480. https://doi.org/10.1038/s41550-023-02096-5

Thomas, E. M., Stallard, T. S., Melin, H., Chowdhury, M. N., Moore, L., O'Donoghue, J., et al. (2025). Auroral and non-auroral H3+ ion winds at Uranus with Keck-NIRSPEC and IRTF-iSHELL. *Geophysical Research Letters*, *52*(7), e2024GL112001. https://doi.org/10.1029/2024GL112001

Tikhonov, A., & Arsenin, V. Y. (1977). Solutions of ill-posed problems.

Tiranti, P. I. (2025). Dataset for JWST discovers the vertical structure of Uranus' ionosphere [Dataset]. *Zenodo*. https://doi.org/10.5281/zenodo.17036022

Tiranti, P. I., Melin, H., Moore, L., Knowles, K., Stallard, T., O'Donoghue, J., et al. (2025). Pole-to-Pole vertical ionospheric profiles at Jupiter from JWST. *Journal of Geophysical Research: Space Physics*, *130*(8), e2025JA034066. https://doi.org/10.1029/2025JA034066

Trafton, L., Geballe, T., Miller, S., Tennyson, J., & Ballester, G. (1993). Detection of H3+ from Uranus. *Astrophysical Journal, Part 1*, *405*, 761–766. https://doi.org/10.1086/172404

Trafton, L., & Kaplan, K. (2025). High spectral resolution observations of Uranus' near-IR thermospheric H2 emission spectrum using the IGRINS spectrograph during the 2018 and 2023 apparitions. *Icarus*, *429*, 116453. https://doi.org/10.1016/j.icarus.2024.116453

Trafton, L., Miller, S., Geballe, T., Tennyson, J., & Ballester, G. (1999). H2 Quadrupole and H3+ emission from Uranus: The Uranian thermosphere, ionosphere, and aurora. *The Astrophysical Journal*, *524*(2), 1059–1083. https://doi.org/10.1086/307838

Tyler, G., Sweetnam, D., Anderson, J., Campbell, J., Eshleman, V., Hinson, D., et al. (1986). Voyager 2 radio science observations of the Uranian system: Atmosphere, rings, and satellites. *Science*, *233*(4759), 79–84. https://doi.org/10.1126/science.233.4759.79

Uno, T., Kasaba, Y., Tao, C., Sakanoi, T., Kagitani, M., Fujisawa, S., et al. (2014). Vertical emissivity profiles of Jupiter's northern H3+ and H2 infrared auroras observed by Subaru/IRCS. *Journal of Geophysical Research: Space Physics*, *119*(12), 10–219. https://doi.org/10.1002/2014JA020454

19448007, 2026, 4, Downloaded from https://agupubs.onlinelibrary.wiley.com/doi/10.1029/2025GL119304 by Cochrane Russian Federation, Wiley Online Library on [19/02/2026]. See the Terms and Conditions (https://onlinelibrary.wiley.com/terms-and-conditions) on Wiley Online Library for rules of use; OA articles are governed by the applicable Creative Commons License